Electric field-dependent scaling law for overdamped (di)electrowetting and dewetting on dielectric

Shreyank Goel, Rakshith Gowda BT, and Dipin S. Pillai*
NICE Group, Department of Chemical Engineering, Indian Institute of Technology Kanpur, Uttar Pradesh 208016, India

(Received 23 May 2024; accepted 10 December 2024; published 8 January 2025; corrected 8 January 2026)

Equilibrium droplet shape and transient dynamics during (di)electrowetting and dewetting on dielectric are electric field–dependent. We present a lubrication model incorporating the Young–Lippmann law that accurately predicts the equilibrium droplet shape and its transient dynamics. The droplet contact line position x_{cl} follows a field-dependent power law $x_{cl} \propto t^n$, where the magnitude of n increases with the applied electric field. When the field strength equals the critical value required for complete wetting, the electrospreading dynamics reduce to the classical Tanner's law ($n = 1/7$), in agreement with past experiments. The magnitude of n for electrodewetting is shown to be greater compared with wetting, attributed to a lesser viscous dissipation in the former case. Despite a difference in the power-law exponent n, the transient dynamics for both (di)electrowetting and electrodewetting are shown to follow the Cox–Voinov law. These observations qualitatively extend beyond the lubrication regime to large contact-angle droplets as well, as confirmed using Navier–Stokes simulations.

DOI: 10.1103/PhysRevFluids.10.014201

I. INTRODUCTION

The wettability of sessile droplets can be altered by modifying the liquid-substrate surface energy using an external electric field, which can be realized in the form of electrowetting, dielectrowetting, or electrodewetting. The phenomenon of electrowetting and electrodewetting is attributed to the principle of electrocapillarity proposed by Lippmann [1]. He discovered that when an external electric field is applied, the interfacial tension is reduced due to the accumulation of charges at the liquid–dielectric interface. The equilibrium contact angle is then described by the classical Young–Lippmann (Y–L) law. Dielectrowetting, on the other hand, is governed by the principle of dielectrophoresis, wherein electromechanical forces generated through polarization of a dielectric material in a nonuniform electric field results in enhanced spreading [2–5]. Electrospreading of a dielectric droplet through dielectrophoresis was first shown by Brown *et al.* [2]. Subsequently, McHale *et al.* [3] proposed a modified Y–L law for dielectrowetting that relates the contact angle to the applied electric potential. Both electrowetting and dielectrowetting are means of tuning wettability; however, the fundamental difference between the two lies in their mechanisms. While dielectrowetting is driven by polarization of the dipoles within the liquid droplet, electrowetting is driven by polarization within the dielectric layer underlying the droplet [3,6]. Additionally, dielectrowetting does not exhibit contact-angle saturation, in contrast to electrowetting [4]. The contact-angle alteration across different configurations (e.g., electrowetting, dielectrowetting, or electrodewetting on dielectric [EWOD, DEW, and EDOD, respectively]) follows the appropriate

*Contact author: dipinsp@iitk.ac.in

form of the Y–L law, which describes the relationship between the apparent contact angle and the applied electric field. This law, however, does not address the transient dynamics involved in the wetting and dewetting processes [7].

The spreading and retracting dynamics of electrified droplets are not only important for fundamental insights, such as the nature of interaction between liquids and substrates [8] and the mechanics of energy dissipation [9], but also for advancements in various technological applications [10]. The electric field–driven manipulation of a sessile droplet has found practical utility in diverse fields of applications such as electrovariable lenses [11,12], reflective displays [13,14], high-power energy harvesting [15], bioassays [16], and many more. The phenomenal rise in electrospreading and retracting-based applications can be ascribed to its superior attributes, spanning from low switching speed to its remarkable ability to actively control individual droplets [17]. Past studies [7,10,18,19] have revealed that electrowetting dynamics can be divided into two regimes: underdamped and overdamped. In the former, dynamics are controlled by a balance between inertial and electrical forces, while in the latter, they are driven by a balance of electrical and viscous forces. The droplet transiting toward its final steady state is monotonic or oscillatory in the overdamped or underdamped regime, respectively. The specific regime observed in an experiment is strongly determined by the droplet size and viscosity [7]. Recently, Xiao and Wu [10] developed a free energy–based theoretical model to predict the droplet dynamics in both regimes for the EWOD configuration. Several biological samples used in electric field–assisted digital microfluidic assays are indeed viscous in nature (e.g., blood, mucus, saliva, and cellular suspensions). Therefore, it is imperative to pursue fundamental investigations in the overdamped regime to improve these applications, and for scenarios where oscillations are undesirable [11,13]. Furthermore, a difference in the dynamic response between electrowetting and dewetting using different liquids and substrates has been experimentally highlighted [9,20]. The findings of Wang *et al.* [20] showed an asymmetry between electrowetting and dewetting, revealing that electrodewetting occurs faster than wetting. In addition, experimental [6] and molecular-simulation [21] studies have shown that electrospreading follows an electric field–dependent power law. McHale *et al.* [6] studied dielectrowetting dynamics and identified that, when the applied voltage equals the critical voltage required for complete wetting, the spreading dynamics precisely follow Tanner's law.

While past research has predominantly concentrated on experiments, we present a unified theoretical framework based on thin-film modeling to elucidate the dynamics of electrowetting, dielectrowetting and electrodewetting on dielectric. The thin-film modeling technique [22] has been extensively used for understanding the physics behind electrified sessile droplets in diverse scenarios. Yeo *et al.* [23] modeled electrostatic surgery of a slender droplet under a parallel-plate electrode configuration using a spatially varying electric field. Wray *et al.* [24,25] studied electrostatic suppression of the coffee-ring effect. Corbett and Kumar [26] studied the spreading dynamics of a droplet flowing down on an inclined plane under a similar electrode configuration. Pillai *et al.* [27] studied the spreading dynamics of a leaky dielectric droplet under periodic forcing. Kainikkara *et al.* [28] showed that a two-dimensional leaky dielectric droplet model predicts qualitatively similar physics as a three-dimensional model at a much-reduced computational cost. Goel and Pillai [29,30] explored the role of bulk and surface charges in surfactant-mediated electrowetting. Chu *et al.* [31] developed a thin-film model for an open-needle electrode configuration to study the ionic surfactant-mediated electrodewetting dynamics. Recently, Pillai and Sahu [32] delineated a universal scaling law for the transient dynamics of contact line motion of highly wetting electrified droplets.

Both EWOD and DEW configurations are designed to enhance the wettability of a droplet under an electric field. EWOD employs a conducting droplet, while a dielectric droplet is used in the case of DEW. EWOD, designed by Berge [17], is one of the most popular configurations and is shown schematically in Fig. 1(a). In this configuration, an electrode is immersed into a conducting droplet, which rests on another electrode coated with a thin dielectric layer. The application of an electric field results in enhanced wetting in the EWOD configuration due to charge buildup under the droplet within the dielectric and the associated decrease in the droplet-substrate surface energy

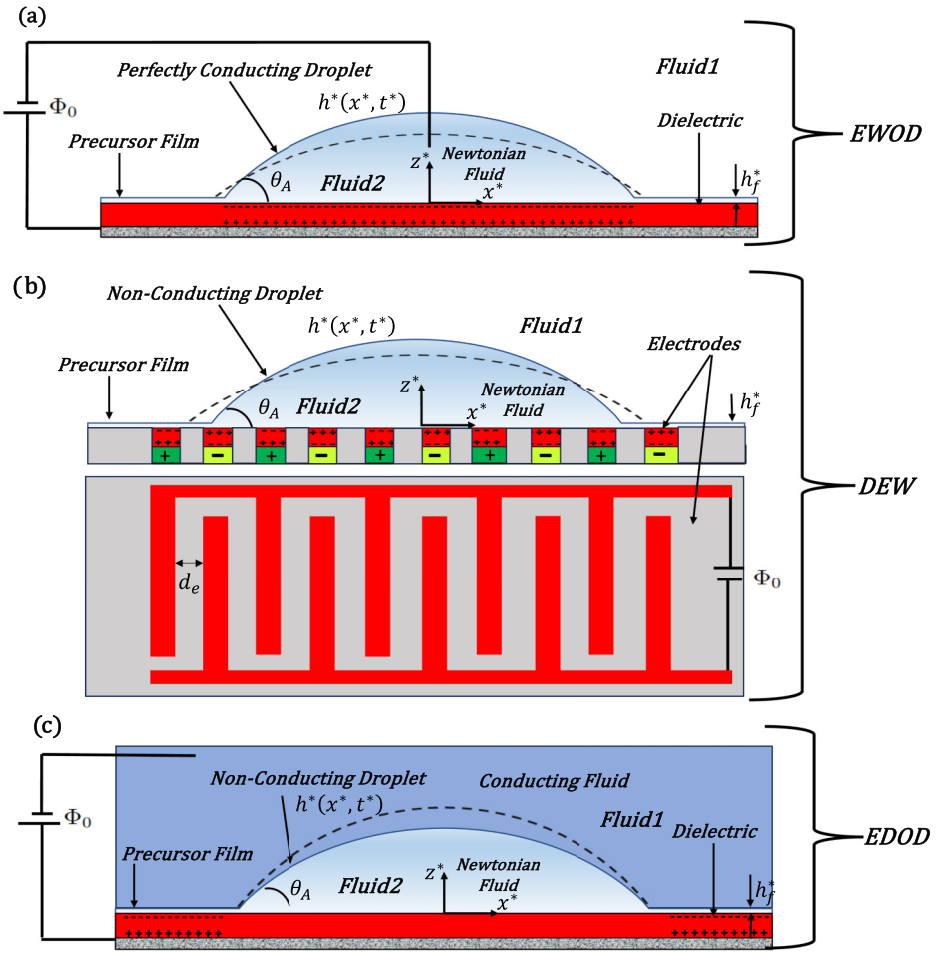

FIG. 1. Schematic of a sessile droplet under an applied electric field for the case of (a) electrowetting on dielectric, (b) dielectrowetting, and (c) electrodewetting on dielectric configurations.

[cf. Fig. 1(a)]. Unlike EWOD, in the DEW configuration, a dielectric droplet rests over a pair of dielectric-coated interdigitated electrodes, as shown in Fig. 1(b). The interdigitated electrodes produce a nonuniform electric field, which polarizes the droplet and results in enhanced spreading due to the net electromechanical force generated [3,6]. In the case of the EDOD configuration [11,20], as shown in Fig. 1(c), one of the electrodes is immersed in the ambient conducting fluid, while the dielectric droplet rests over another electrode coated with a thin dielectric layer. In this configuration, dewetting takes place due to charge buildup within the dielectric outside the triple-phase contact line, and the associated reduction in the substrate–ambient fluid interfacial energy [cf. Fig. 1(c)]. We develop a lubrication model to predict the spatiotemporal dynamics of droplet contact line motion under these configurations. This is the first time the Frumkin–Derjaguin theory is coupled with Y–L law in a consistent framework to derive the lubrication model for EWOD, DEW, and EDOD configurations. Using the lubrication model, we first analytically obtain the electric field–dependent steady-state contact angle for these configurations. The obtained analytical expression is shown to match the low contact angle limit of the Y–L law. Subsequently, transient simulations are performed to elucidate the electric field–dependent power-law dependence of contact line motion. In agreement with the experiments of McHale *et al.* [33], the contact

line motion is shown to exactly follow the Tanner's law for the critical electrical field, leading to complete wetting. Electrodewetting dynamics are shown to be faster than electrowetting dynamics, in line with the experiments of Wang *et al.* [20]. Finally, despite this difference, both electrowetting and dewetting are shown to obey the Cox–Voinov law, which is in line with past experimental studies [9].

II. MATHEMATICAL MODEL FOR EWOD, DEW, AND EDOD

We consider a two-dimensional sessile droplet marked *Fluid2* for EWOD, EDOD, and DEW configurations. The ambient fluid is denoted by *Fluid1,* as shown in Fig. 1. Kainikkara *et al.* [28] have shown that a two-dimensional thin-film droplet model gives qualitatively similar predictions at a much reduced computational cost compared with the three-dimensional thin-film model. Herein, *Fluid1* is assumed to be mechanically passive, that is, at a constant pressure and exerting no hydrodynamic stress on *Fluid2* other than this constant pressure. This is a reasonable approximation for the EWOD configuration, where *Fluid2* is usually air. However, for the EDOD configuration, this assumption holds true only if the ratio of ambient fluid viscosity to droplet viscosity is sufficiently small. Even if the ambient viscosity is significant, it affects only the transient dynamics, and the steady-state solution remains unchanged. *Fluid2* is a Newtonian fluid having mass density ρ and viscosity μ. The interfacial tension of the *Fluid1–Fluid2* interface is γ. Evaporative effects are ignored. The droplet is assumed to be surrounded by a thin precursor film to overcome the contact-line singularity [34–38]. A Cartesian coordinate system (x^*, z^*) is considered, where x^* represents the horizontal direction and z^* denotes the vertical direction. The origin is located at the center of the wetted diameter, just beneath the droplet. Also, u^* and w^* are the horizontal and vertical components of the velocity vector $\vec{v}^*$ for *Fluid2*. For EWOD and EDOD configurations, a dielectric layer [shown in red in Fig. 1(a,c)] of thickness d and electrical permittivity ε_d is sandwiched between the droplet and the bottom electrode. In the case of EWOD, as depicted in Fig. 1(a), *Fluid2* is considered to be a perfect conductor, while *Fluid1* is taken to be a perfect dielectric. The top electrode is then dipped into the conducting *Fluid2,* ensuring that net polarization of the dielectric remains confined within the droplet-wetted area. However, in EDOD, as shown in Fig. 1(c), *Fluid2* is considered to be a perfect dielectric, while *Fluid1* is a perfect conductor. The top electrode is then plunged in *Fluid1*, which leads to the net polarization of dielectric being outside the droplet-wetted area. Φ_0 is the potential drop applied across the two electrodes. Lastly, in the case of DEW, as shown in Fig. 1(b), *Fluid2* is considered to be a perfect dielectric. Here, a nonuniform electric field is generated using an interdigitated electrode. The permittivity of dielectric *Fluid2* in DEW is taken to be ε_2, and d_e represents the spacing between the two electrodes.

A. Governing equations

The droplet flow fields $(p^*, \vec{v}^*)$ are governed by the standard continuity and Navier–Stokes equations, given as

$$\nabla^* \cdot \vec{v}^* = 0 \quad \text{and} \quad \rho\left(\frac{\partial \vec{v}^*}{\partial t^*} + \vec{v}^* \cdot \nabla^* \vec{v}^*\right) = -\nabla^* p^* + \mu \nabla^{*2} \vec{v}^*. \tag{1}$$

The *fluid1–fluid2* interface is located at $z^* = h^*(x^*, t^*)$, where the stress free condition gives

$$\vec{n}^* \cdot T^* \cdot \vec{t}^* = 0, \quad \text{with} \quad \vec{n}^* = \frac{-\frac{\partial h^*}{\partial x^*}\hat{e}_x + \hat{e}_z}{\sqrt{1 + \left(\frac{\partial h^*}{\partial x^*}\right)^2}} \quad \text{and} \quad \vec{t}^* = \frac{\hat{e}_x + \frac{\partial h^*}{\partial x^*}\hat{e}_z}{\sqrt{1 + \left(\frac{\partial h^*}{\partial x^*}\right)^2}}. \tag{2}$$

In the previous equations, $\mathbf{T}^* = -p^*\mathbf{I} + \mu(\nabla^*\vec{v}^* + \nabla^*\vec{v}^{*T})$ represents the Newtonian stress tensor, $\vec{n}^*$ is the normal unit vector, $\vec{t}^*$ is the tangential unit vector, and $\hat{e}_x$ and $\hat{e}_z$ denote the unit basis vectors in the x^* and z^* directions, respectively. The normal stress balance at the interface is

given by

$$\vec{n}^* \cdot T^* \cdot \vec{n}^* = -\gamma \nabla_s^* \cdot \vec{n}^* + \Pi(h^*), \tag{3}$$

where the first term on the right-hand side corresponds to the capillary pressure. The last term denotes the disjoining-conjoining pressure, given as

$$\Pi(h^*) = \left(\frac{A}{h_0^{*3}}\right)\left[\frac{h_0^{*3}}{h^{*3}} - \frac{h_0^{*2}}{h^{*2}}\right]. \tag{4}$$

Here, A/h_0^{*3} represents the Hamaker constant with h_0^* being the film thickness that minimizes the conjoining-disjoining potential $U(h^*) = -\int \Pi(h^*)dh^*$. The first and second terms on the right-hand side of Eq. (4) represent repulsive and attractive interactions, respectively. The Young–Dupré equation relates the field-free apparent contact angle (θ_0) to the *Fluid1–Fluid2* (γ), droplet–dielectric (γ_{2d}), and *Fluid1*–dielectric (γ_{1d}) interfacial tensions, as given by $\cos\theta_0 = \frac{\gamma_{1d}-\gamma_{2d}}{\gamma}$. The Frumkin–Derjaguin theory [39] relates the three interfacial tensions with the conjoining-disjoining potential, by accounting for the work done against this potential in taking the film thickness from $h^* = h_0^*$ to $h^* \to \infty$ as

$$\int_{h_0^*}^{\infty} \Pi(h^*)dh^* = \gamma_{1d} - \gamma - \gamma_{2d}. \tag{5}$$

In the case of EWOD, the application of an electric field polarizes the dielectric under the droplet and leads to a decrease in *Fluid2*–dielectric interfacial tension, given by $\gamma_{2d} - e^*$, where e^* is the change in interfacial tension due to the applied electric field. We assume here that the dielectric interface has no adsorbed charges in the absence of an electric field [17]. The modified form of Frumkin–Derjaguin equation (5) for EWOD configuration thus becomes

$$\int_{h_0^*}^{\infty} \Pi(h^*)dh^* = \gamma_{1d} - \gamma - \gamma_{2d} + e^*. \tag{6}$$

Substituting for $\Pi(h^*)$ from Eq. (4) into Eq. (6), we obtain the Hamaker parameter A, in terms of the wetting parameter $s \equiv \gamma + \gamma_{2d} - \gamma_{1d} = \gamma(1 - \cos\theta_0)$ and e^*, as

$$A = 2h_0^{*2}(s - e^*). \tag{7}$$

The quantity $e^* = C\Phi_0^2/2$ for both cases of EWOD and DEW, with the only difference being that $C = \varepsilon_d\varepsilon_0/d$ for the case of EWOD and $C = \varepsilon_0(\varepsilon_2 - 1)\pi/4d_e$ for the case of DEW, as theoretically shown by McHale *et al.* [3].

For the case of EDOD, as the dielectric polarization upon application of an electric field occurs outside the wetted radius, it leads to a decrease in $fluid1 - dielectric$ interfacial tension, as given by $\gamma_{1d} - e^*$. Herein, $e^* = C\Phi_0^2/2$ with $C = \varepsilon_d\varepsilon_0/d$. This leads to the modification of the Frumkin–Derjaguin equation (5) to yield

$$\int_{h_0^*}^{\infty} \Pi(h^*)dh^* = \gamma_{1d} - e^* - \gamma - \gamma_{2d}. \tag{8}$$

Hence, the relation between A, s, and e^* can be obtained using Eqs. (8) and (4) as

$$A = 2h_0^{*2}(s + e^*). \tag{9}$$

Equations (7) and (9) can be combined into a generalized form valid across all configurations as

$$A = 2h_0^{*2}(s - E^*) \quad \text{with} \quad \begin{cases} E^* = \frac{C\Phi_0^2}{2}, & \text{where } C = \varepsilon_d\varepsilon_0/d & \text{for EWOD,} \\ E^* = \frac{C\Phi_0^2}{2}, & \text{where } C = \varepsilon_0(\varepsilon_2 - 1)\pi/4d_e & \text{for DEW,} \\ E^* = -\frac{C\Phi_0^2}{2}, & \text{where } C = \varepsilon_d\varepsilon_0/d & \text{for EDOD.} \end{cases} \tag{10}$$

Here, C is the specific capacitance within the dielectric layer for the case of EDOD and EWOD, and inside dielectric droplet for the case of DEW that accounts for the dielectric polarization following the appropriate form of the Y–L law, given as

$$\cos\theta = \cos\theta_0 + \frac{C\Phi_0^2}{2\gamma}. \tag{11}$$

The previous equation relates the apparent contact angle (θ) to the imposed external electric field. It is a combination of Young–Dupré law, which relates the zero-field apparent contact angle (θ_0) to that of the three interfacial energies and Lippmann's theory of electrocapillarity [1]. Substituting for A from Eq. (10) into Eq. (4), we get

$$\Pi(h^*) = \left(\frac{2(s-E^*)}{h_0^*}\right)\left[\frac{h_0^{*3}}{h^{*3}} - \frac{h_0^{*2}}{h^{*2}}\right]. \tag{12}$$

Therefore, Eq. (3) becomes

$$\vec{n}^* \cdot T^* \cdot \vec{n}^* = -\gamma \nabla_s^* \cdot \vec{n}^* + \left(\frac{2(s-E^*)}{h_0^*}\right)\left[\frac{h_0^{*3}}{h^{*3}} - \frac{h_0^{*2}}{h^{*2}}\right]. \tag{13}$$

Also, as the *Fluid1–Fluid2* interface is a material surface, the kinematic condition is applied. The no-slip and no-penetration conditions are applied at the bottom dielectric–*Fluid2* interface. These are given as

$$w^*\big|_{z^*=h^*} = \frac{\partial h^*}{\partial t^*} + u^*\big|_{z^*=h^*}\frac{\partial h^*}{\partial x^*}, \quad \text{and} \quad u^*(x,0,t) = 0 \text{ and } w^*(x,0,t) = 0. \tag{14}$$

B. Thin-film model

The governing equations are nondimensionalized using the following scaling based on the thin-film approximation ($\delta = H/\Lambda \ll 1$): $x^* = \Lambda x$, $z^* = Hz$, $u^* = (U)u$, $w^* = (\delta U)w$, $t^* = (\Lambda/U)t$, $p^* = (\mu U/\delta H)p$. Here, H corresponds to the centerline height of the equilibrium droplet under zero electric field, and Λ is the droplet's wetted diameter. The characteristic pressure scale used here is the viscous pressure scale, suitable for the overdamped regime. Also, the capillary number $Ca = \frac{\mu U}{\gamma}$ is chosen to be $\mathcal{O}(\delta^3)$, such that the characteristic velocity becomes $U = \delta^3\gamma/(3\mu)$. The gravitational effects are ignored, assuming that Bond number $Bo = \rho g \Lambda^2/\gamma \ll 1$. The lubrication approximation is employed such that $\delta^2 \ll 1$ and $Re\delta \ll 1$, where $Re = \rho U H/\mu$ is the Reynolds number. This approximation is valid for small contact-angle droplets. After scaling the governing equations and retaining $\mathcal{O}(1)$ terms, the Navier–Stokes equation in x and z direction, tangential stress [Eq. (2)] and normal stress [Eq. (13)] boundary conditions become

$$\frac{\partial p}{\partial x} = \frac{\partial^2 u}{\partial z^2}, \quad \frac{\partial p}{\partial z} = 0, \quad \left.\frac{\partial u}{\partial z}\right|_{z=h} = 0, \quad \text{and} \quad p|_{z=h} = -3\left(\frac{\partial^2 h}{\partial x^2} + \frac{2(S-E)}{h_0}\left[\frac{h_0^3}{h^3} - \frac{h_0^2}{h^2}\right]\right). \tag{15}$$

Here, $S = \frac{s}{\delta^2\gamma}$ represents the wettability number and $E = \pm\frac{C\Phi_0^2}{2\delta^2\gamma}$ represents the electrowetting number. We then integrate the z momentum equation and eliminate pressure using the x-momentum equation and the normal stress balance [Eq. (15)]. Thereafter, the no-slip and no-penetration boundary conditions [Eq. (14)] are used to solve for the velocity field. The velocity field is then substituted into the kinematic condition [Eq. (14)] to get the final evolution equation as

$$\frac{\partial h}{\partial t} + \frac{\partial}{\partial x}\left(h^3\frac{\partial^3 h}{\partial x^3}\right) + \frac{2(S-E)}{h_0}\frac{\partial}{\partial x}\left(h^3\frac{\partial}{\partial x}\left[\left(\frac{h_0}{h}\right)^3 - \left(\frac{h_0}{h}\right)^2\right]\right) = 0. \tag{16}$$

Having obtained the lubrication model by dropping higher-order terms, we can now rescale Eq. (16) by setting $\delta = 1$. This procedure corresponds to obtaining the dimensional form of the simplified

lubrication model [Eq. (16)] that was obtained, and then using a single characteristic length scale H to scale length in both directions. In the rescaled Eq. (16) thus obtained, the dimensionless numbers become $S = \frac{s}{\gamma}$ and $E = \pm\frac{C\Phi_0^2}{2\gamma}$. Thus, the lubrication parameter δ helps to explicitly gauge the relative significance of each term in the governing equations and boundary conditions and conveniently truncates the model at the required order. The Y–L equation (11) in terms of the nondimensional number E then becomes

$$\cos\theta = \cos\theta_0 + E, \tag{17}$$

where $E > 0$ corresponds to the EWOD or DEW configurations and $E < 0$ corresponds to the EDOD configuration.

III. RESULTS AND DISCUSSION

We begin by presenting the analytical solution for the steady-state apparent contact angle in the presence of an electric field using the lubrication model. It will be shown that the result agrees well with the low-angle approximation of the Y–L law [Eq. (17)].

A. Analytical solution for contact angle under electric field

The apparent contact angle of the sessile droplet can be obtained by solving the lubrication model [Eq. (16)] for the steady-state solution, leading to a balance between the capillary and disjoining-conjoining pressures under the electric field, as given by

$$\frac{\partial}{\partial x}\left(h^3\frac{\partial^3 h}{\partial x^3} + \frac{2(S-E)}{h_0}h^3\frac{\partial}{\partial x}\left[\left(\frac{h_0}{h}\right)^3 - \left(\frac{h_0}{h}\right)^2\right]\right) = 0. \tag{18}$$

After integrating Eq. (18) twice from a point x, where the interface position is h, to $x \to \infty$, where the precursor film thickness at steady state is h_f, we obtain

$$\frac{\partial^2 h}{\partial x^2} + \frac{2(S-E)}{h_0}\left[\left(\frac{h_0}{h}\right)^3 - \left(\frac{h_0}{h}\right)^2\right] = \frac{2(S-E)}{h_0}\left[\left(\frac{h_0}{h_f}\right)^3 - \left(\frac{h_0}{h_f}\right)^2\right]. \tag{19}$$

In obtaining this equation, we have made use of the fact that all spatial derivatives of the film thickness are zero in the precursor film (i.e., at $x \to \infty$). Integrating Eq. (19) further with respect to x, we get the steady-state droplet contact angle θ, defined as the angle at the point of inflection [37], that is, where $h_{xx} = 0$, given as

$$h_x = \tan\theta = \sqrt{2(S-E)f(h_f, h_0)}, \tag{20}$$

where,

$$f(h_f, h_0) = \frac{h_f^2 - 12h_f h_0 + 9h_0^2 + \sqrt{(h_f + 3h_0)(h_f - h_0)}(3h_0 + h_f)}{-2h_f^2}. \tag{21}$$

Equation (20) represents the analytical solution for the apparent contact angle in the presence of an electric field. It must be noted that the precursor film thickness h_f need not equal h_0 and is not known *a priori*. Gomba and Homsy [37] have shown that h_f is bounded and of the same order of magnitude as h_0, with $h_0 < h_f < 1.5h_0$. However, the exact value of h_f can only be determined numerically. For large aspect ratio droplets upholding the validity of lubrication approximation, calculations reveal that ($h_f/h_0 \approx 1$ and $f(h_f, h_0) \approx 1$) and Eq. (20) simplifies to

$$\tan\theta = \sqrt{2(S-E)}. \tag{22}$$

Equation (22) represents the approximate analytical solution for low contact angles. For small contact angles, $\theta < 11^\circ$, $\tan^2\theta \approx 2(1-\cos\theta)$, and Eq. (22) recovers the Y–L law given by Eq. (17). However, for moderate or large contact angles, this approximation does not hold true, and the error

between contact angles predicted by Eqs. (17) and (22) can become significant (e.g., for $\theta = 30^\circ$, the error using this approximation becomes as large as 24%.) It must be noted that, although there are two parameters, S and E, the steady-state contact angle, given by both Eqs. (21) and (22), depends solely on the combination $(S - E)$, which we term the effective wettability number.

B. Numerical solution for thin-film model

The electric field–free equilibrium droplet profile is obtained by running a transient simulation of the evolution equation [Eq. (16)] with $E = 0$. The initial and boundary conditions used for this case are as follows:

$$h|_{x,t=0} = \begin{cases} h_0, & |x| > 1, \\ (1 - h_0)x^4 + 2(h_0 - 1)x^2 + 1, & |x| \leqslant 1, \end{cases} \quad \text{and} \quad \frac{\partial^n h}{\partial x^n}(x = -L, t) = \frac{\partial^n h}{\partial x^n}(x = L, t). \tag{23}$$

Here, h_0 is taken to be 10^{-4}, and the boundary conditions are considered to be spatially periodic, with $n = 0, 1, 2, 3$. Further, L denotes the half-length of the computational domain, taken to be 8. The initial condition and domain size are chosen to ensure that large aspect ratio droplets are obtained that uphold the validity of the lubrication model. The second-order finite difference method in conservative form with spatially periodic boundary conditions is used to maintain a higher-order spatial resolution. The number of grid points per unit domain length N is chosen to be 625 for all calculations, ensuring grid independence, and the time integration is performed using the NDSolve subroutine in Wolfram Mathematica 13.0. After obtaining the field-free equilibrium profile, it is then utilized in subsequent simulations as the initial condition to investigate the impact of the electric field.

In Fig. 2(a), the apparent contact angle θ is plotted on the vertical axis with electrowetting number E on the horizontal axis for the EWOD/DEW configuration ($E > 0$). The numerically obtained steady-state solution from the lubrication model [Eq. (16)] is compared with the classical Y–L law [Eq. (17)] as well as the approximate analytical solution obtained in Eq. (22). It can be seen that the lubrication model prediction is in good agreement with the classical Y–L equation. The minor discrepancy observed between the numerical solution and the Y–L law is attributed to the assumption that h_f/h_0 was taken to be unity in the analytical derivation, whereas in the numerical computations, $h_f/h_0 \approx 1$. The numerical result, thus, exactly matches the analytical expression given by Eq. (20) once the numerically obtained precursor film thickness h_f is substituted. The decrease in contact angle observed from Fig. 2(a) and the steady-state droplet profile plotted in Fig. 2(b) confirm enhanced spreading with electrowetting number. This electrospreading behavior is caused by a decrease in the effective wettability number $(S - E)$ with an increase in electrowetting number E. This analysis confirms that the lubrication model [Eq. (16)] successfully accounts for the presence of dielectric polarization within the wetted radius, resulting in a reduction in liquid–dielectric interfacial tension, thereby leading to electrowetting.

In Fig. 2(c), the temporal variation of the droplet's contact line position x_{cl} is plotted for different values of E as it reaches its steady state. For spreading to occur (contact line position to increase), the electrostatic forces have to overcome the viscous resistance offered by the precursor film. The spreading dynamics thus are characterized by the dominance of electrostatic forces over the viscous dissipation near the contact line. In this regime, x_{cl} follows a power-law relationship, given as $x_{cl} \propto t^n$. Importantly, the magnitude of the power-law exponent n increases with an increase in E and approaches that of the classical Tanner's law for complete wetting given by $n = 1/7$ [40]. In fact, Fig. 2(d) depicts the case when the electric field strength equals the threshold value required for complete wetting, that is, when $E = S$. It is evident from the figure that the transient dynamics exactly adhere to Tanner's law with $n = 1/7$, qualitatively matching the experimental observations of McHale *et al.* [6]. The exponent n is plotted with E in Fig. 2(e) for two values of S. It can be seen that n increases with E, showing a steeper rise at higher values of E. Additionally, for a given value of E, a droplet with a higher S exhibits a greater value of n. In the thin-film model

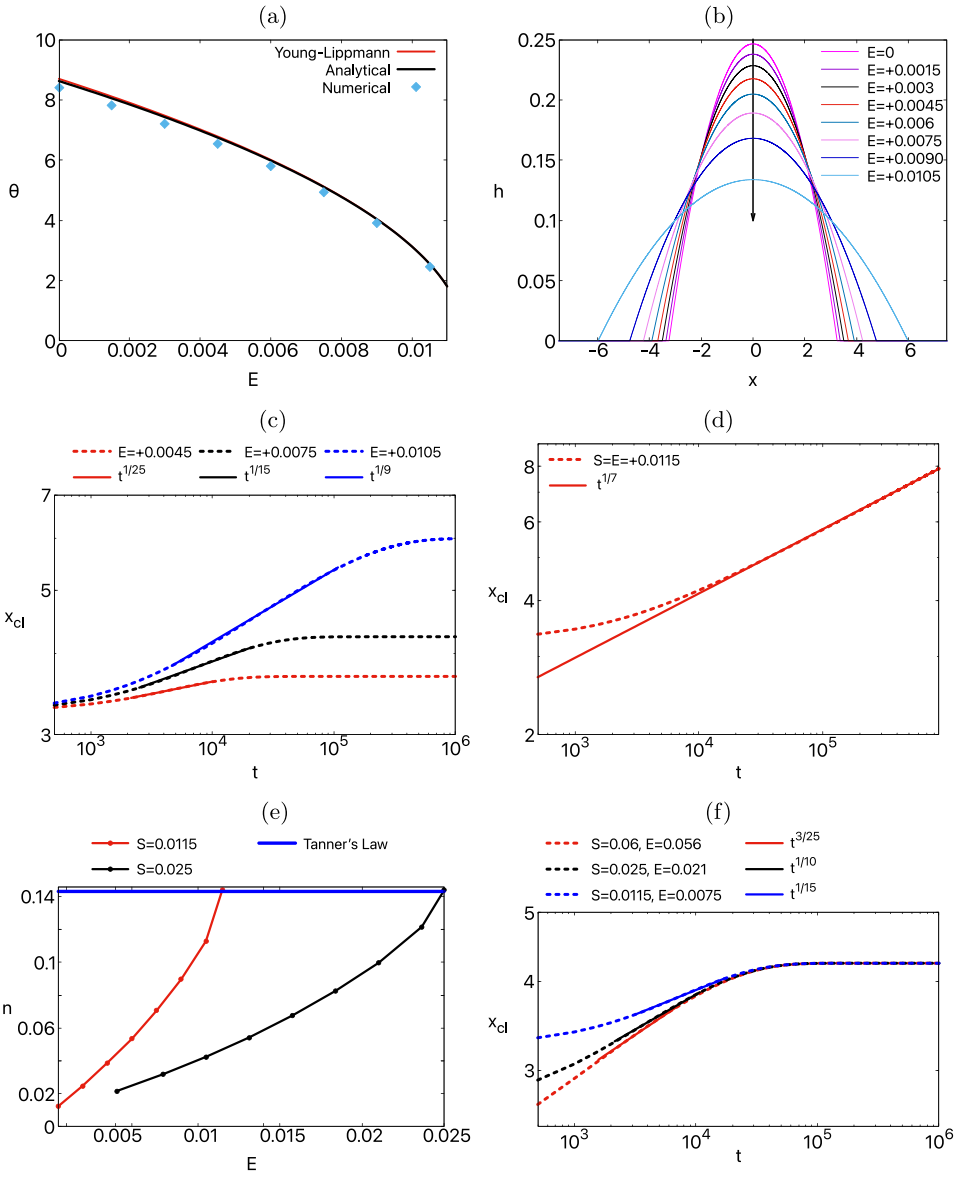

FIG. 2. (a) The apparent contact angle (degree) is plotted with electrowetting number E for the (di)electrowetting on dielectric configuration ($E > 0$). (b) Steady-state droplet profile for different E and (c) temporal dynamics of the contact line position x_{cl} exhibiting a electric field–dependent power law. (d) The temporal dynamics of contact line position x_{cl} for the case of critical electric field strength needed for complete wetting follows Tanner's law with $n = 1/7$. The value of the wettability number S is taken to be 0.0115 for the panels (a)–(d). (e) The exponent of electric field–dependent power law n is plotted with E. (f) Temporal dynamics of the contact line position x_{cl} exhibiting an electric field–dependent power law for three different electric field–free contact angles (characterized by S), but having the same value of $(S - E)$. The value of initial film thickness is taken to be $h_0 = 0.0001$ for panels (a)–(f).

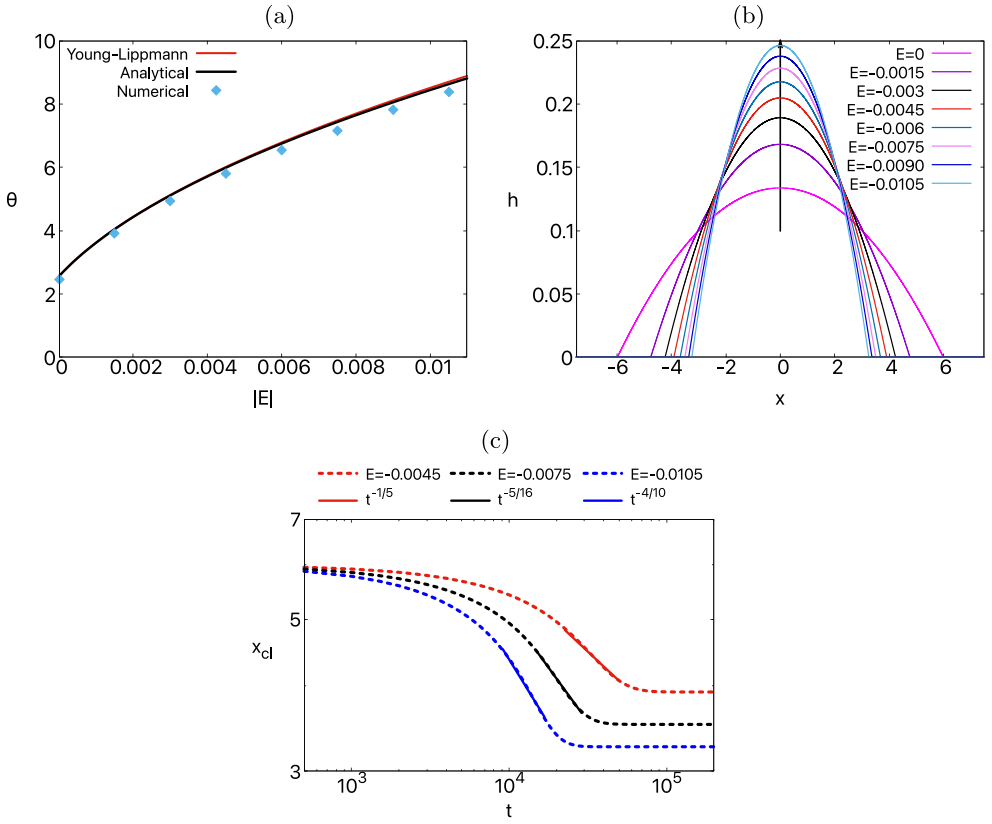

FIG. 3. (a) The apparent contact angle (degree) is plotted with the magnitude of electrowetting number E for the electrodewetting on dielectric configuration ($E < 0$). (b) Steady-state droplet profile for different E and (c) temporal dynamics of the contact line position x_{cl} exhibiting electric field–dependent power law. The value of h_0 and wettability number S are taken to be 0.0001 and 0.001, respectively.

given by Eq. (16), the parameters S and E appear as a combination $(S - E)$. This suggests that the combination $(S - E)$ might uniquely determine the droplet's spatiotemporal evolution. However, it is essential to note that the governing equation must be accompanied by an initial condition, specifically, the initial droplet profile in the absence of an electric field. This initial profile is dictated by the value of S. Therefore, even if $(S - E)$ remains constant, the dynamics will vary depending on the specific value of S. This is exemplified in Fig. 2(f), where the electric field–dependent power law is depicted for three different initial contact angles, characterized by S, but keeping $(S - E)$ constant. A constant $(S - E)$ implies that these droplets attain the same final configuration across all three cases. The magnitude of the power-law exponent is proportional to the increase in the initial contact angle (or an increaes in S). This is apparent from the fact that the electric field strength must increase to achieve the same final equilibrium contact angle.

Next, for the EDOD configuration ($E < 0$), we explore the dewetting dynamics under the imposed electric field. In Fig. 3(a), the apparent contact angle θ for such a case is plotted on the vertical axis with the magnitude of electrowetting number E on the horizontal axis. The lubrication model accurately reproduces the electrodewetting described by the Y–L law (with $E < 0$). Again, the minor discrepancy between the numerically obtained θ and the Y–L law is attributed to $h_0/h_f \approx 1$. The increase in contact angle observed in Fig. 3(a) and the steady-state droplet profile plotted in Fig. 3(b) confirm enhanced dewetting with an increase in the magnitude of electrowetting number. This

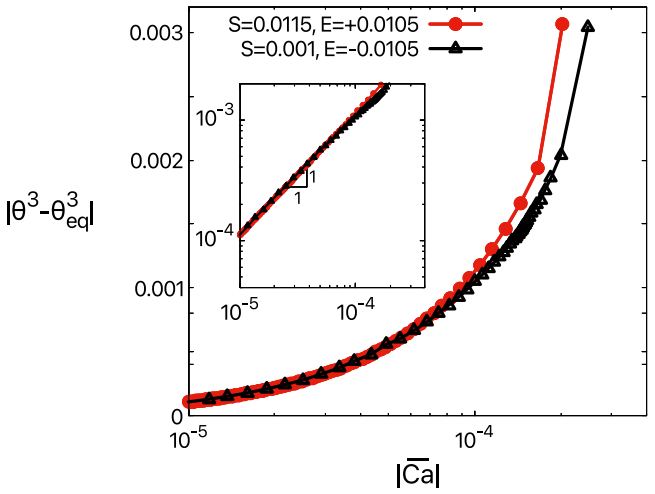

FIG. 4. $|\theta^3 - \theta_{eq}^3|$ is plotted with $|\overline{Ca}|$ for the (di)electrowetting, and electrodewetting on dielectric configurations with $h_0 = 0.0001$.

dewetting behavior is caused due to an increase in the effective wettability number $(S - E)$, with the magnitude of electrowetting number E. In Fig. 3(c), the temporal variation of the droplet's contact line position x_{cl} is plotted for different E. For dewetting to occur (contact line position to decrease), the electrostatic forces have to overcome the viscous resistance offered by the droplet bulk, and x_{cl} follows an electric field–dependent power-law relationship $x_{cl} \propto t^{-n}$, where n increases with the magnitude of E. A higher value of n results in faster dynamics for fixed E. It is to be noted that the magnitude of n is higher for EDOD compared with EWOD/DEW for the same magnitude of E, indicating an asymmetry between the dynamics of electrowetting and dewetting. This observation aligns with the experimental findings of Wang *et al.* [20], who showed that electrodewetting occurs at a faster rate compared with wetting over hydrophilic substrates. This asymmetry is attributed to the lesser magnitude of bulk viscous dissipation experienced in the case of dewetting compared with the dissipation within the precursor film near the contact line experienced during the wetting process [41]. Further, the results of the lubrication model reveal that, despite the asymmetry in the power-law exponent n between the EWOD/DEW and EDOD configurations, both follow the generalized Cox–Voinov relationship (cf. Fig. 4). As per the Cox–Voinov theory, the contact line dynamics are described by $|\theta^3 - \theta_{eq}^3| \propto |\overline{Ca}|^{\beta}$, where $\overline{Ca} = v_{cl}$ denotes the capillary number defined in terms of the dimensionless contact line velocity v_{cl}. Figure 4 shows that both electrowetting and electrodewetting follow the Cox–Voinov law, akin to previous theoretical [42] and experimental findings [9].

C. Navier–Stokes simulations

In the previous section, a simple model developed using the lubrication theory coupled with Lippmann's theory of electrocapillarity was developed to accurately predict the dynamics of (di)electrowetting and dewetting for small contact angle droplets. Nevertheless, a majority of experiments are conducted using high contact angle droplets. For such droplets, the only way to predict their dynamics is to carry out full Navier–Stokes simulations. Toward this, the droplet hydrodynamics are numerically solved using continuity and Navier–Stokes equations given by Eq. (1) in COMSOL Multiphysics 6.0. A moving mesh method is supplemented with contact angle boundary conditions at the intersection of the free surface and wall using the laminar flow module. The dielectric is considered to be a slipping wall, with a specified contact angle, determined by the

Y–L equation (17), and written in terms of S and E as

$$\theta = \cos^{-1}[1 - (S - E)]. \tag{24}$$

In the laminar flow module, the stress balance at the *Fluid1–Fluid2* interface is given by

$$\vec{n}_1^* \cdot T^* = (\gamma \nabla_s^* \cdot \vec{n}_1^*)\vec{n}_1^*. \tag{25}$$

Here, $\vec{n}_1^*$ represents the unit normal at the moving (*Fluid1–Fluid2*) interface, pointing toward *Fluid2*. Note that $\vec{n}_1^*$ points in the opposite direction of n^* defined in Sec. II A. The kinematic boundary condition at the moving interface is given by

$$\vec{v}_{\text{mesh}}^* \cdot \vec{n_1}^* = \vec{v}^* \cdot \vec{n_1}^*, \tag{26}$$

where, $\vec{v}_{\text{mesh}}^*$ represents the mesh velocity at the interface. The wall boundary condition at the *Fluid2*–dielectric interface is given by

$$\vec{n_1}^* \cdot T^* \cdot \vec{t_1}^* = -\frac{\mu}{\beta}(\vec{v}^* - (\vec{v}^* \cdot \vec{n_1}^*)\vec{n_1}^*) \quad \text{and} \quad \vec{v}^* \cdot \vec{n}_{\text{wall}}^* = 0. \tag{27}$$

In the previous, the first equation represents the Navier-slip condition, which is used to relax the stress singularity at the contact line with β denoting the slip length. The second equation corresponds to a no-penetration boundary condition, where $\vec{n}_{\text{wall}}^*$ represents the normal at the *Fluid2*–dielectric interface. Further details of the simulations are given in the Appendix.

In Fig. 5(a), the steady-state apparent contact angle θ is plotted with the electrowetting number E for the EWOD/DEW configuration ($E > 0$). It is evident from the figure that the results obtained from Navier–Stokes simulations are in excellent agreement with the classical Y–L law [Eq. (17)]. Akin to the low contact angle droplets, Fig. 5(b) reveals that x_{cl} follows a power-law relationship, given as $x_{cl} \propto t^n$, wherein the magnitude of the power-law exponent n increases with an increase in E. Further, Fig. 5(c) illustrates the scenario where the electric field strength equals the threshold needed for complete wetting, clearly showing that the transient dynamics in this complete wetting case adhere to Tanner's law. The exponent obtained from full Navier–Stokes simulations is 1/6, consistent with the Navier–Stokes simulation results reported by Mahady *et al.* [42]. A slight discrepancy is noted between the Tanner's law exponent obtained from full Navier–Stokes simulations and that from the thin-film model. This difference arises because the classically derived exponent assumes lubrication approximation conditions, which may not apply to full Navier–Stokes simulations. The power-law exponent increases almost linearly with E, as depicted in Fig. 5(d). The conclusions for the EWOD/DEW configuration, as obtained from full Navier–Stokes simulations, are in agreement with the contact line dynamics predicted by the thin-film model presented in the previous section.

Next, we explore the dewetting dynamics for the EDOD configuration ($E < 0$) using full Navier–Stokes simulations. In Fig. 6(a), the apparent contact angle θ for such a case is plotted on the vertical axis with the magnitude of electrowetting number E on the horizontal axis. It is evident from the figure that the full Navier–Stokes simulations accurately reproduce the electrodewetting behavior as described by the Y–L law with $E < 0$. The contact angle increases with an increase in the magnitude of the electrowetting number, indicating enhanced dewetting. In Fig. 6(b), the temporal variation of the droplet's contact line position x_{cl} is plotted for different E. As in the previous section, it is evident that x_{cl} follows an electric field–dependent power-law relationship, $x_{cl} \propto t^{-n}$, where n increases with the magnitude of E. Furthermore, Navier–Stokes simulations also reveal that the magnitude of n is higher for EDOD compared with EWOD/DEW for the same magnitude of E, indicating an asymmetry between electrowetting and dewetting. This asymmetry is further illustrated by the velocity contours plotted for both cases at two time instants in Figs. 7(a)–7(d). The droplet reaches its steady state more quickly in the EDOD case compared with EWOD/DEW, as evident from the almost zero velocity (approaching steady state) in Figs. 7(c) and 7(d) compared with Figs. 7(a) and 7(b).

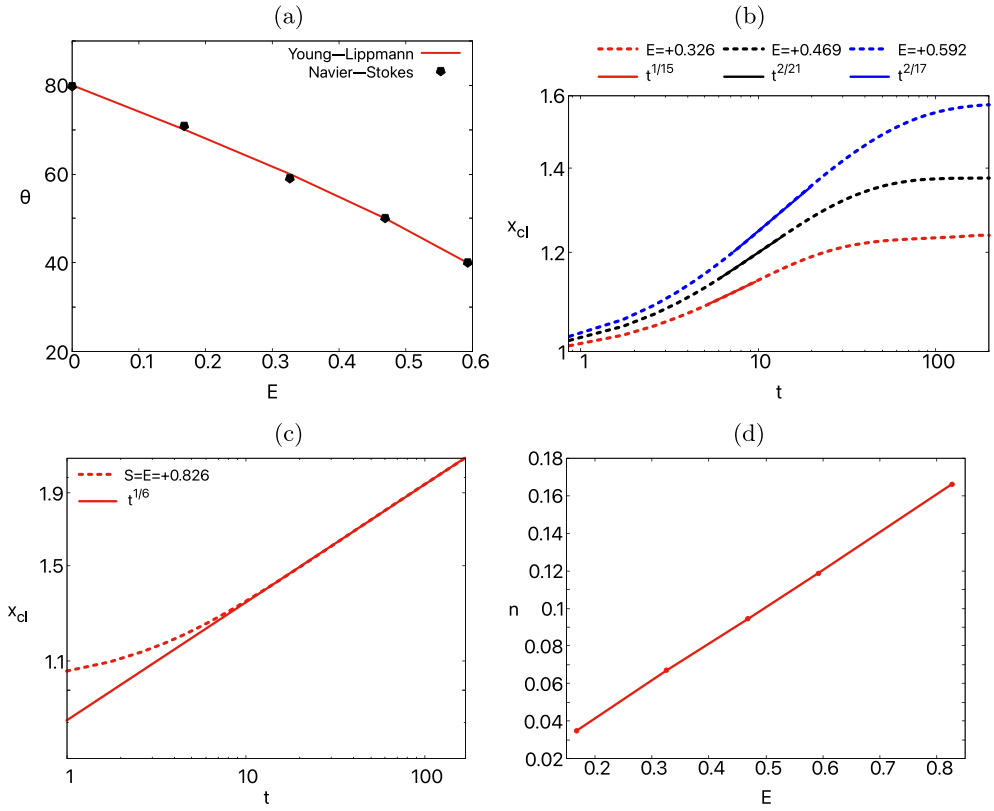

FIG. 5. (a) The apparent contact angle (degree) is plotted with the magnitude of electrowetting number, E for (di)electrowetting on dielectric configuration ($E > 0$), (b) Temporal variation of the contact line position, x_{cl}, exhibiting electric field–dependent power law. (c) Temporal variation of contact line position x_{cl}, for the case of the critical electric field needed for complete wetting, follow Tanner's law with $n = 1/6$. (d) The exponent of electric field dependent power law, n is plotted with E. The value of wettability number S is taken to be 0.826.

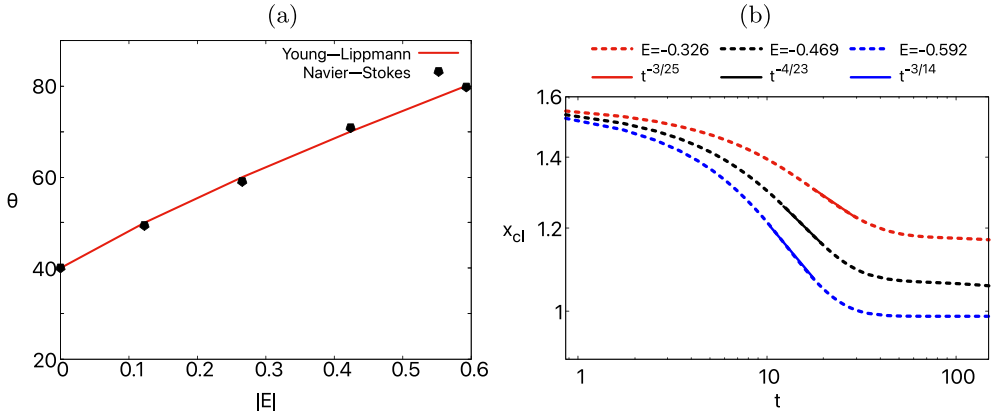

FIG. 6. (a) The apparent contact angle (degree) is plotted with the magnitude of electrowetting number E for the electrodewetting on dielectric configuration ($E < 0$). (b) Temporal dynamics of the contact line position x_{cl} exhibiting electric field–dependent power law. The wettability number S is taken to be 0.234.

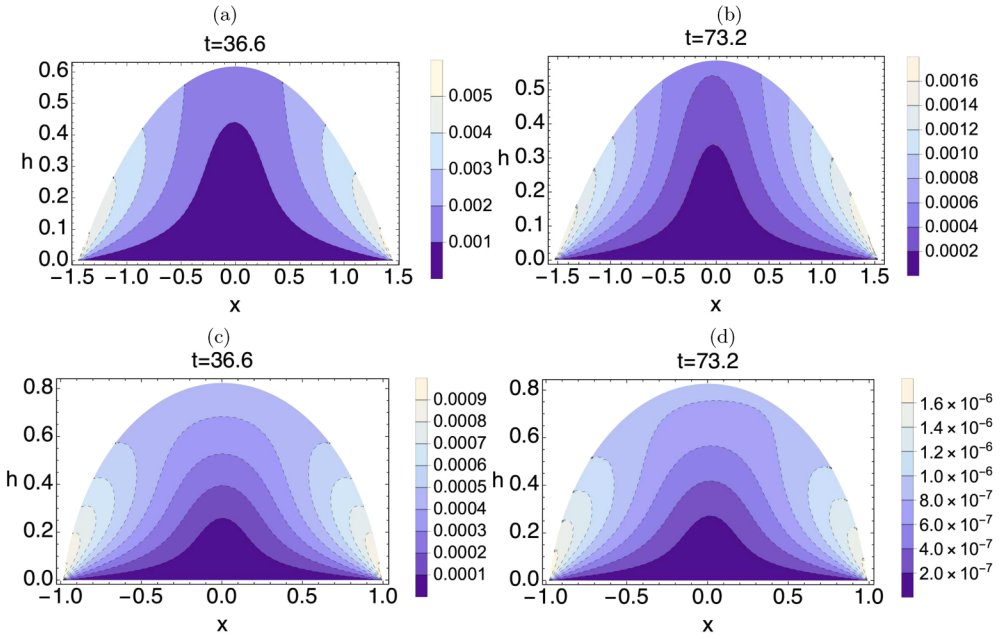

FIG. 7. Velocity contours are plotted at different time instants for the case of (a), (b) (di)electrowetting, and (c), (d) electrodewetting on dielectric. The values of $(S,\ E)$ for electrowetting, dielectrowetting, and electrodewetting on dielectric are taken to be $(0.826,\ 0.592)$, and $(0.234,\ -0.592)$, respectively.

IV. CONCLUSIONS

A thin-film lubrication model incorporating the Y–L law was developed to model the dynamics of EWOD/EDOD and DEW in the overdamped regime. An analytical solution was obtained for the steady-state contact angle for both EWOD/DEW and EDOD configurations and was shown to match the low contact angle approximation of the Y–L law. The contact line position of the droplet follows an electric field–dependent power law, with its exponent increasing with an increase in the magnitude of the electrowetting number. Electrowetting for the critical field strength corresponding to complete wetting follows Tanner's law exactly with a power-law exponent of 1/7. An asymmetry in the power-law exponent is observed between electrowetting and electrodewetting dynamics for the same magnitude of electrowetting number. The electrodewetting exponent was found to be higher than electrowetting, which is attributed to lesser viscous dissipation in the latter case. Despite this asymmetry, calculations reveal that the contact line dynamics for all the EWOD, EDOD, and DEW configurations obey the Cox–Voinov law. Additionally, the analysis of electric field–dependent scaling law for contact line dynamics was extended to the case of large contact angles using full Navier–Stokes simulations.

ACKNOWLEDGMENTS

We are grateful to Ministry of Education, India, for providing funding through Prime Minister's Research Fellowship (2301355), and the Science and Engineering Research Board (SERB), India (CRG/2023/008432), for their financial support.

The authors report no conflict of interest.

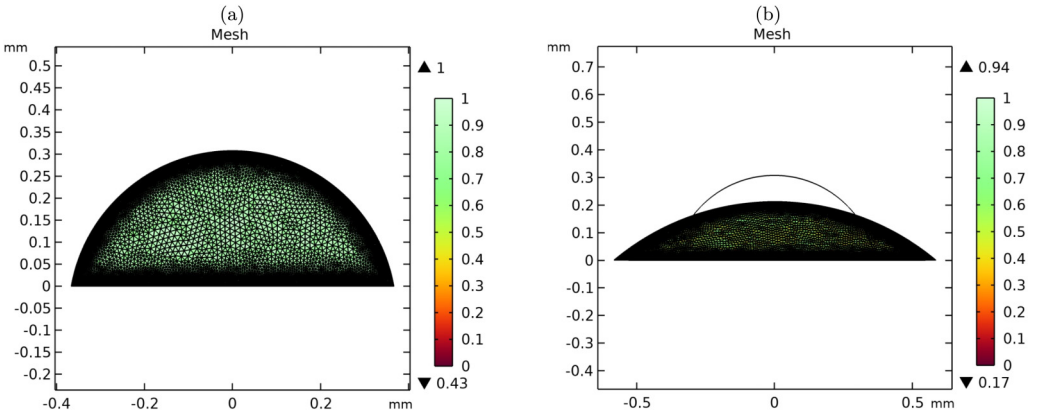

FIG. 8. Droplet geometry with mesh contours corresponding to $nG = 1364$ are plotted for (a) initial and (b) final steady state corresponding to electrowetting and dielectrowetting on dielectric. The S and E values for electrowetting and dielectrowetting on dielectric are taken to be 0.826 and 0.592, respectively.

APPENDIX: DETAILS OF NAVIER–STOKES SIMULATIONS

The governing equations in Sec. C are solved in dimensional form supplemented with initial conditions where the electric field–free droplet profile is considered part of a circle, as shown in Fig. 8(a). The initial droplet profile is obtained by slicing a circle of radius R_1 at a vertical distance of $R_1 \cos\theta_0$ its center. Thus, the droplet profile is given by

$$z = \sqrt{{R_1}^2 - x^2} + R_1 \cos\theta_0 \quad \text{and} \quad z \geqslant 0, \tag{A1}$$

where $R_1 \sin\theta_0$, $R_1(1 - \cos\theta_0)$ and θ_0 represent initial spreading radius, height, and electric field–free equilibrium contact angle of the droplet. The area of the droplet can be calculated as $A = {R_1}^2(\theta_0 - \cos\theta_0 \sin\theta_0)$, which is held constant at 0.169 mm^2 for all simulations. The simulations of EWOD/DEW are performed using the electric field—free equilibrium droplet shape corresponding to $S = 0.826$. To keep our analysis consistent across all simulations of EWOD/DEW and EDOD,

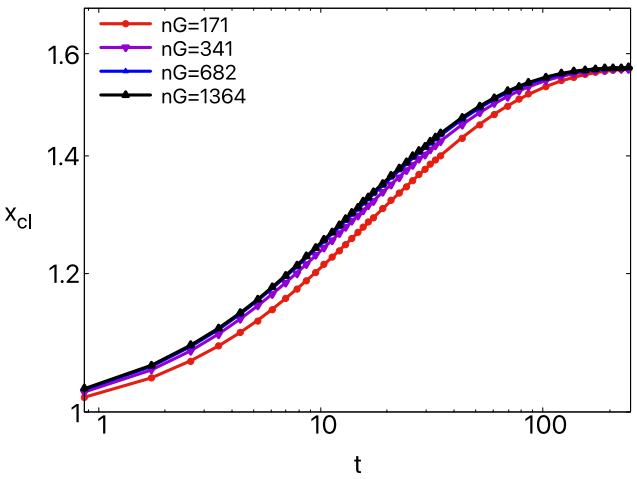

FIG. 9. Temporal variation of the contact line position x_{cl} for different grid points at the *fluid2*–air and *fluid2*–solid interfaces. The S and E values are taken to be 0.826 and 0.592, respectively.

we use the final equilibrium shape of EWOD, which was found with $S = 0.826$, $E = 0.5924$, as the starting point for all EDOD simulations. The parameters used in the simulations correspond to 1, 2 propylene glycol, whose density, viscosity, and surface tension are 1032 kg/m^3, 0.056 Pa s, and 0.036 N/m, respectively. The slip length at the bottom substrate is taken to be 0.372 μm. To enhance accuracy while minimizing computing cost, a denser mesh is employed near the interface compared with the bulk droplet, as shown in Fig. 8. In all simulations, the characteristic length and time scale are taken to be $R_1 = 0.371$ mm and $R_1/U = 0.578$ ms, respectively. The grid independence test, as shown in Fig. 9, was conducted by adjusting the total number of grid points at the *Fluid2*–air and *Fluid2*–solid interfaces, denoted as nG, while keeping a maximum mesh size of 0.094 per unit characteristic length in the bulk. The root mean-squared error between $nG = 682$ and $nG = 1364$ was $0.2\% \ll 1$, ensuring grid independence with minimal computational cost.

[1] M. G. Lippmann, Relations Entre les Phénomènes Électriques et Capillaires, Ann. Chim. Phys. **5**, 494 (1875).

[2] C. Brown, G. Wells, M. Newton, and G. McHale, Voltage-programmable liquid optical interface, Nat. Photon. **3**, 403 (2009).

[3] G. McHale, C. V. Brown, M. I. Newton, G. G. Wells, and N. Sampara, Dielectrowetting driven spreading of droplets, Phys. Rev. Lett. **107**, 186101 (2011).

[4] A. M. Edwards, C. V. Brown, M. Newton, and G. McHale, Dielectrowetting: The past, present and future, Curr. Opin. Colloid Interface Sci. **36**, 28 (2018).

[5] A. M. Edwards, R. Ledesma-Aguilar, M. I. Newton, C. V. Brown, and G. McHale, Electrostatic control of dewetting dynamics, Appl. Phys. Lett. **116**, 253703 (2020).

[6] G. McHale, C. Brown, and N. Sampara, Voltage-induced spreading and superspreading of liquids, Nat. Commun. **4**, 1605 (2013).

[7] Q. Vo, H. Su, and T. Tran, Universal transient dynamics of electrowetting droplets, Sci. Rep. **8**, 836 (2018).

[8] Q. Vo and T. Tran, Droplet jumping by modulated electrowetting, J. Fluid Mech. **977**, A24 (2023).

[9] H. Li, M. Paneru, R. Sedev, and J. Ralston, Dynamic electrowetting and dewetting of ionic liquids at a hydrophobic solid–liquid interface, Langmuir **29**, 2631 (2013).

[10] K. Xiao and C.-X. Wu, Droplet dynamics driven by electrowetting, Phys. Rev. E **105**, 064609 (2022).

[11] B. Berge and J. Peseux, Variable focal lens controlled by an external voltage: An application of electrowetting, Eur. Phys. J. E **3**, 159 (2000).

[12] C.-C. Cheng, C. A. Chang, and J. A. Yeh, Variable focus dielectric liquid droplet lens, Opt. Express **14**, 4101 (2006).

[13] R. A. Hayes and B. J. Feenstra, Video-speed electronic paper based on electrowetting, Nature (London) **425**, 383 (2003).

[14] H. You and A. Steckl, Three-color electrowetting display device for electronic paper, Appl. Phys. Lett. **97**, 023514 (2010).

[15] T. Krupenkin and J. A. Taylor, Reverse electrowetting as a new approach to high-power energy harvesting, Nat. Commun. **2**, 448 (2011).

[16] M. J. Jebrail, M. S. Bartsch, and K. D. Patel, Digital microfluidics: A versatile tool for applications in chemistry, biology and medicine, Lab. Chip. **12**, 2452 (2012).

[17] F. Mugele and J. C. Baret, Electrowetting: From basics to applications, J. Phys.: Condens. Matter **17**, R705 (2005).

[18] J. Hong, Y. K. Kim, K. H. Kang, J. M. Oh, and I. S. Kang, Effects of drop size and viscosity on spreading dynamics in dc electrowetting, Langmuir **29**, 9118 (2013).

[19] Q. Vo and T. Tran, Contact line friction of electrowetting actuated viscous droplets, Phys. Rev. E **97**, 063101 (2018).

[20] Q. Wang, M. Xu, C. Wang, J. Gu, N. Hu, J. Lyu, and W. Yao, Actuation of a nonconductive droplet in an aqueous fluid by reversed electrowetting effect, Langmuir **36**, 8152 (2020).
[21] Q. Yuan and Y.-P. Zhao, Precursor film in dynamic wetting, electrowetting, and electro-elasto-capillarity, Phys. Rev. Lett. **104**, 246101 (2010).
[22] A. Oron, S. H. Davis, and S. G. Bankoff, Long-scale evolution of thin liquid films, Rev. Mod. Phys. **69**, 931 (1997).
[23] L. Yeo, R. Craster, and O. Matar, Drop manipulation and surgery using electric fields, J. Colloid Interface Sci. **306**, 368 (2007).
[24] A. W. Wray, D. T. Papageorgiou, R. V. Craster, K. Sefiane, and O. K. Matar, Electrostatic suppression of the "coffee stain effect", Langmuir **30**, 5849 (2014).
[25] A. W. Wray, D. T. Papageorgiou, R. V. Craster, K. Sefiane, and O. K. Matar, Electrostatic suppression of the "coffee-stain effect", Procedia IUTAM **15**, 172 (2015).
[26] A. Corbett and S. Kumar, Spreading of thin droplets of perfect and leaky dielectric liquids on inclined surfaces, Langmuir **32**, 6606 (2016).
[27] D. S. Pillai, K. C. Sahu, and R. Narayanan, Electrowetting of a leaky dielectric droplet under a time-periodic electric field, Phys. Rev. Fluids **6**, 073701 (2021).
[28] M. A. Kainikkara, D. S. Pillai, and K. C. Sahu, Equivalence of sessile droplet dynamics under periodic and steady electric fields, NPJ Microgravity **7**, 47 (2021).
[29] S. Goel and D. S. Pillai, Electrokinetic thin-film model for electrowetting: The role of bulk charges, Langmuir **39**, 13076 (2023).
[30] S. Goel and D. S. Pillai, Reduced-order model for surfactant-laden electrified sessile droplets, Langmuir **39**, 15177 (2023).
[31] W. Chu, H. Ji, Q. Wang, C.-J. C. Kim, and A. L. Bertozzi, Electrohydrodynamics modeling of droplet actuation on a solid surface by surfactant-mediated electrodewetting, Phys. Rev. Fluids **8**, 073701 (2023).
[32] D. S. Pillai and K. C. Sahu, Universal scaling law for electrified sessile droplets on a lyophilic surface, Phys. Rev. E **109**, L013101 (2024).
[33] G. McHale, B. V. Orme, G. G. Wells, and R. Ledesma-Aguilar, Apparent contact angles on lubricant-impregnated surfaces/SLIPS: From superhydrophobicity to electrowetting, Langmuir **35**, 4197 (2019).
[34] P. G. De Gennes, Wetting: statics and dynamics, Rev. Mod. Phys. **57**, 827 (1985).
[35] V. S. Mitlin and N. V. Petviashvili, Nonlinear dynamics of dewetting: Kinetically stable structures, Phys. Lett. A **192**, 323 (1994).
[36] L. W. Schwartz and R. R. Eley, Simulation of droplet motion on low-energy and heterogeneous surfaces, J. Colloid Interface Sci. **202**, 173 (1998).
[37] J. M. Gomba and G. M. Homsy, Analytical solutions for partially wetting two-dimensional droplets, Langmuir **25**, 5684 (2009).
[38] J. M. Gomba and G. M. Homsy, Regimes of thermocapillary migration of droplets under partial wetting conditions, J. Fluid Mech. **647**, 125 (2010).
[39] N. Churaev and V. Sobolev, Prediction of contact angles on the basis of the Frumkin-Derjaguin approach, Adv. Colloid Interface Sci. **61**, 1 (1995).
[40] L. Tanner, The spreading of silicone oil drops on horizontal surfaces, J. Phys. D **12**, 1473 (1979).
[41] J. G. Petrov, J. Ralston, M. Schneemilch, and R. A. Hayes, Dynamics of partial wetting and dewetting in well-defined systems, J. Phys. Chem. B **107**, 1634 (2003).
[42] K. Mahady, S. Afkhami, J. Diez, and L. Kondic, Comparison of Navier-Stokes simulations with long-wave theory: Study of wetting and dewetting, Phys. Fluids **25**, 112103 (2013).

Correction: A typographical error in the text below Eq. (19) has been fixed. An incorrect version of Figure 4 was used for publication and has now been replaced with the correct version.